ACS APPLIED MATERIALS & INTERFACES

Research Article

www.acsami.org

Structure-Independent Proton Transport in Cerium(III) Phosphate Nanowires

Péter Pusztai,[†] Henrik Haspel,[†] Ildikó Y. Tóth,[‡] Etelka Tombácz,[‡] Krisztina László,[§] Ákos Kukovecz,[†,∥] and Zoltán Kónya*[,†,⊥]

[†]Department of Applied and Environmental Chemistry, University of Szeged, Rerrich Béla tér 1., H-6720 Szeged, Hungary

[‡]Department of Physical Chemistry and Materials Science, University of Szeged, Aradi Vértanúk tere 1., H-6720 Szeged, Hungary

[§]Department of Physical Chemistry and Materials Science, Budapest University of Technology and Economics, H-1521 Budapest, Hungary

[∥]MTA-SZTE "Lendület" Porous Nanocomposites Research Group, Rerrich Béla tér 1., H-6720 Szeged, Hungary

[⊥]MTA-SZTE Reaction Kinetics and Surface Chemistry Research Group, Rerrich Béla tér 1., H-6720 Szeged, Hungary

Supporting Information

ABSTRACT: Understanding of water-related electrical conduction is of utmost importance in applications that utilize solid-state proton conductors. However, in spite of the vast amount of theoretical and experimental work published in the literature, thus far its mechanism remained unsolved. In this study, the structure-related ambient temperature electrical conduction of one-dimensional hydrophilic nanostructures was investigated. Cerium phosphate nanowires with monoclinic and hexagonal crystal structures were synthesized via the hydrothermal and ambient temperature precipitation routes, and their structural and surface properties were examined by using high-resolution transmission electron microscopy, X-ray diffractometry, nitrogen and water sorption, temperature-programmed ammonia desorption, and potentiometric titration techniques. The relative humidity (RH)-dependent charge-transport processes of hexagonal and monoclinic nanowires were investigated by means of impedance spectroscopy and transient ionic current measurement techniques to gain insight into their atomistic level mechanism. Although considerable differences in RH-dependent conductivity were first found, the distinct characteristics collapsed into a master curve when specific surface area and acidity were taken into account, implying structure-independent proton conduction mechanism in both types of nanowires.

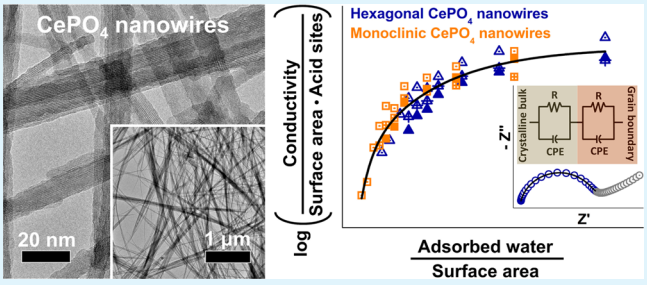

KEYWORDS: *proton conduction, cerium phosphate, master curve, impedance spectroscopy, surface acidity, fuel cell membrane*

1. INTRODUCTION

The reform of global energy management became an urgent task in our continuously developing world. By the early 1970s, the concept of hydrogen economy emerged as an alternative approach to replace fossil-fuel economy.[1−3] However, some ultimate stipulations have to be satisfied, first, to make this paradigm shift in energy management come true.

A crucial step in the commercialization of fuel cells is the precise design of their electrolyte. Proton-exchange membrane fuel cells (PEMFCs) have the potential for the most widespread application from powering ordinary electric devices to providing new generation automotive propulsion. Because of the polymeric origin of the membrane in PEMFCs, they are unlikely to work at operating temperatures higher than 100 °C as that would infer structural stability issues. To overcome this limitation, hygroscopic oxide and heteropoly acid incorporated membranes with enhanced structural stability were tested that can retain water even at elevated temperatures.[4,5] Structural stability can further be improved by mixing inorganic nanoparticles into the polymeric matrix[6] or by replacing the polymeric matrix itself with inorganic skeletons or metal−organic frameworks.

Concerning proton conduction, at relatively low operating temperatures the Grotthuss proton hopping and the so-called vehicle mechanisms were commonly proposed.[7−11] To ensure the most efficient operation of these mechanisms, precisely designed membranes are required. For this purpose phosphoric/phosphonic acid functionalized or phosphate based membranes emerged as very promising candidates.[10,12−14] Phosphate groups on the surface serve both as proton donors and as proton acceptors by self-dissociation. This promotes the formation of a dynamic hydrogen-bonded network, providing high proton conductivity even at elevated temperatures in the absence of water. The replacement of polymeric matrixes by more stable solid acid proton conductors like phosphates (zirconium and titanium phosphates, cesium dihydrogen

Received: March 12, 2015
Accepted: April 10, 2015
Published: April 10, 2015

DOI: 10.1021/acsami.5b02177
ACS Appl. Mater. Interfaces 2015, 7, 9947−9956

phosphate, and also tin or cerium pyrophosphate)[15−20] is also a subject of ongoing research.

It was previously observed that proton conduction is very sensitive to the structure and surface chemistry of the materials.[21−23] Phase transitions at elevated temperatures can change the proton-conducting properties. In the case of zirconium tetraphosphonate coordination polymer, the rearrangement of the crystal structure resulted in a decrease in proton conduction,[24] while cesium dihydrogen phosphate featured a so-called superprotonic transition temperature, above which a marked conduction increase occurred.[20] Structure-dependent proton conduction differences were also indicated for tin pyrophosphates, among which cubic/pseudocubic SnP_2O_7 performed much better than those with layered and amorphous structure.[25]

It was previously proved that lanthanide phosphates may act as proton-conducting membranes, opening way to various practical applications.[26−29] However, many of the publications dealt only with the high-temperature proton conduction of these materials, disregarding their structure-dependent low-temperature conduction behavior. In this study we report the first data on the effect of structural properties on the room-temperature proton conductivity of hexagonal and monoclinic cerium phosphate nanowires. Although primary measurements indicated considerable conductivity differences, factoring surface area and surface acidity differences transformed all data into a single master curve, suggesting that the proton conduction mechanism is structure-independent in both types of nanowires.

2. EXPERIMENTAL SECTION

2.1. Preparation of Hexagonal and Monoclinic Nanowires. All reagents were of analytical grade and used as received. Cerium(III) nitrate hexahydrate was purchased from Sigma-Aldrich. Phosphoric acid and absolute ethanol were purchased from Molar Chemicals Ltd.

Hexagonal and monoclinic nanowires were prepared by two different synthesis methods. For the preparation of hexagonal nanowires a simple room-temperature procedure was applied where 20 mL of 0.2 M phosphoric acid (85%) solution was added dropwise to 60 mL of 0.033 M cerium nitrate solution under vigorous stirring.[30] To obtain monoclinic nanowires, the phosphoric acid solution was added in one step to the cerium nitrate solution. After 20 min of vigorous stirring, the obtained suspension was poured into a poly(tetrafluoroethylene)-lined stainless steel autoclave (120 mL) and was kept at 200 °C for 4 h. At the end of the synthesis both samples were rinsed and centrifuged with deionized water and ethanol thoroughly. The samples were then dried at 40 °C overnight.

2.2. Characterization of the Nanowires. TEM images were taken by using a FEI TECNAI G^2 20 X-Twin high-resolution transmission electron microscope operating at an accelerating voltage of 200 kV. X-ray diffractometry (XRD) was performed at ambient temperature on a Rigaku Miniflex II diffractometer using a Cu Kα radiation source (λ = 0.1542 nm) operating at 30 kV and 15 mA. Diffraction patterns were recorded in the 2θ range of 10−70° at 1°/min scanning rate. The purity of the samples was revealed via energy-dispersive X-ray spectroscopy (EDS) in an Hitachi S-4700 Type II cold field emission scanning electron microscope (SEM) instrument operated at 10 or 20 kV accelerating voltage and equipped with an integrated Röntec QX2 EDS detector. Water sorption behavior of the samples was examined at 20 °C temperature in a Quantachrome Hydrosorb-1000 type water vapor sorption analyzer. The samples were measured in the 0.05−0.90 relative pressure range. The samples were vacuum-degassed at room temperature for 24 h to ensure a water-free surface for the subsequent water sorption measurements. Temperature-programmed desorption (TPD) of ammonia was measured in a BELCAT-A catalyst analyzer. TPD curves were recorded in a helium atmosphere by heating the samples from 40 to 450 °C at a heating rate of 10 °C/min. Prior to ammonia adsorption, the samples were subjected to a blind TPD (from 40 to 400 °C) to eliminate any contamination on the surface of the nanowires. For the electrical conduction study the nanowires were drop-casted onto alumina-supported micropatterned platinum integrated electrodes and placed into sealed vessels containing different saturated salt solutions to ensure various relative humidity conditions in the 6−100 RH% range. Relative humidity is the ratio of the actual vapor pressure (p) of water to the saturated vapor pressure (p_0) at a particular temperature, commonly expressed in percentage ($100 \cdot p/p_0$). The specific surface area (SSA) of the samples was determined by using the well-known Brunauer−Emmett−Teller (BET) equation[31] and its extended counterpart, the Guggenheim−Anderson−de Boer (GAB) equation,[32]

$$m_a = \frac{kacm_{mon}}{(1 - ka)(1 + (c - 1)ka)} \quad (3)$$

where m_a is the amount of water adsorbed on 1 g of $CePO_4$ nanowires at sorbate activity a, m_{mon} is the amount of water needed for the formation of monolayer sorbate coverage over the same unit, c and k are energy constants to account for the variation of the chemical potential of the sorbate molecule in the upper sorption layer and in the monolayer, and in the upper sorption layer and in the bulk, respectively. The GAB equation was created by introducing an additional constant into the BET model. It provides better fit in a considerably wider sorbate activity range (i.e., up to 0.8−0.9 compared to 0.35 of the BET method). At k = 1 the GAB equation reduces to the original BET expression. After the determination of m_{mon} the specific surface area values could be derived according to the following equation,

$$SSA = \frac{m_{mon}N_A A_m}{M} \quad (2)$$

where SSA is the specific surface area of the sample, N_A is the Avogadro constant (6.022×10^{23} 1/mol), A_m is the cross-sectional area of a single water molecule (10.5 Å^2/molecule),[33] and M is the molecular weight of water (18 g/mol).

Room-temperature impedance spectra of the samples were recorded on a Novocontrol Alpha-A frequency response analyzer in the frequency range from 10 mHz to 10 MHz applying a sinusoidal voltage with an amplitude of 1 V (rms). Room-temperature isothermal transient ionic current (ITIC) measurements were performed on a KEITHLEY 2612A SYSTEM Source Meter by using an excitation voltage of 3 V.

2.3. Acid−Base Titrations. Potentiometric acid−base titrations were performed under a CO_2-free atmosphere to characterize the pH- and ionic strength-dependent net proton consumptions of $CePO_4$ by a GIMET1 automatic homemade titrator system.[34] The background electrolyte was 0.005, 0.05, and 0.5 M aqueous NaCl solution. Before titrations, the suspensions were stirred and bubbled with purified nitrogen for 15 min. Titrations under nitrogen bubbling were performed

DOI: 10.1021/acsami.5b02177
ACS Appl. Mater. Interfaces 2015, 7, 9947−9956

continuously, first U (up) titration with 0.1 M NaOH titrant and then D (down) titration back to pH ~ 3 with the 0.1 M HCl titrant. The "up" and "down" labels indicate the direction of pH change. Net proton consumptions were calculated from the mass balance for H^+/OH^- ions, including the determination of their experimental activity coefficients. Data points of the titration results belong to the actual equilibrium states, where the equilibrium criterion of $\Delta pH/min < 0.012$ was chosen.

2.4. Zeta Potential Measurements. Electrophoretic mobilities of the $CePO_4$ dispersions were measured at 25 ± 0.1 °C in a Nano ZS (Malvern) dynamic light-scattering apparatus with a 4 mW He−Ne laser source (λ = 633 nm) using disposable zeta cells (DTS 1060). The zeta-standard of Malvern (−55 ± 5 mV) was used for calibration. The Smoluchowski equation was applied to convert electrophoretic mobilities to zeta potential values. The effect of pH variation (between 3 and 10) on the zeta potential values of the $CePO_4$ nanoparticles was studied at 10 mM NaCl. The accuracy of the measurements was ±5 mV.

3. RESULTS AND DISCUSSION

According to TEM investigation shown in Figure 1, both samples consisted of nanowires a few micrometers in length.

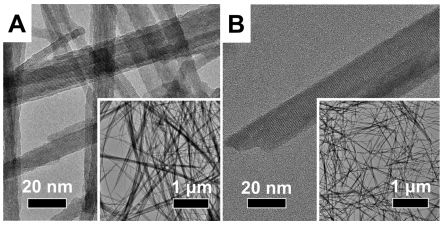

Figure 1. TEM images of micrometer long hexagonal (A) and monoclinic (B) nanowires. In the case of hexagonal nanowires bundle formation was observed. Both hexagonal nanowire bundles and monoclinic nanowires possessed an aspect ratio between 40 and 60. Surface roughness differences between the samples are due to the different synthesis methods and the different resistivity of crystal structures toward an acidic environment.

Hexagonal and monoclinic nanowires have an average diameter of 6.3 ± 2.5 and 15.7 ± 7.0 nm, respectively. The diameter of hexagonal nanowire bundles was in the range of 60−80 nm; however, some bundles with a diameter larger than 100 nm could also be found. The aspect ratios for monoclinic nanowires and hexagonal nanowire bundles were found to be between 40 and 60. To gain better insight into the microscopic surface structure, high-resolution TEM images were taken. According to Figure 1, hexagonal nanowires possessed a rougher surface compared to that of the monoclinic nanowires. This difference in surface roughness may well be associated with the differences in synthesis methods. Hexagonal nanowires had well-crystallized core structure with a discontinuous, roughened surface which may be due to the etching effect of H^+ ions.[35] Hydrothermal synthesis is more advantageous for the enhanced crystallization of the nanowires and the monoclinic crystal structure is more resistant toward an acidic environment;[36,37] hence, a smoother surface developed in the latter case. The different resistivity of hexagonal and monoclinic nanowires toward an acidic environment is also obvious from the potentiometric titration curves discussed below in detail. Under pH ~ 3.5 hexagonal nanowires dissolved conspicuously faster than their monoclinic counterparts.

The X-ray diffractogram displayed in Figure 2 indicated different crystal structures for the two materials synthesized.

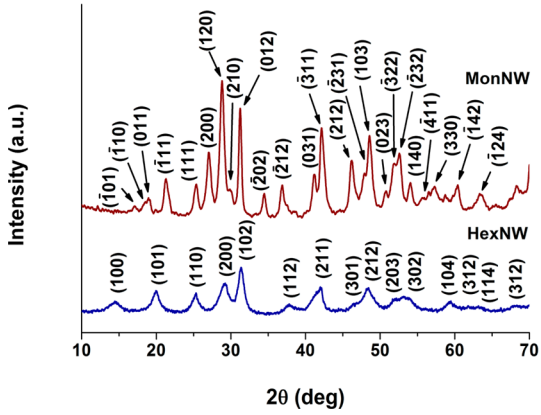

Figure 2. XRD profiles of phase pure hexagonal (a = 7.055 Å and c = 6.439 Å) and monoclinic (a = 6.777 Å, b = 6.993 Å, and c = 6.445 Å) $CePO_4$ nanowires.

Nanowires prepared at room temperature showed pure hexagonal crystal structure with a = 7.055 Å and c = 6.439 Å lattice parameters (JCPDS No. 74-1889). However, elevated temperature and pressure promoted the formation of monoclinic phase with lattice parameters a = 6.777 Å, b = 6.993 Å, and c = 6.445 Å (JCPDS No. 84-0247). Since ionic impurities can significantly alter the electrical conduction of a material, energy-dispersive X-ray spectroscopy was applied to examine the elemental composition and purity of the samples. According to EDS measurements (see Figure S1 in the Supporting Information), the nanowires consisted of only Ce, P, and O without any detectable impurities.

The adsorption characteristics of the nanowires were investigated by nitrogen and water sorption techniques. Nitrogen adsorption−desorption isotherms (see Figure S2 in Supporting Information) featured typical type IV characteristics with type A hysteresis loops. The corresponding BJH pore size distribution (PSD) curves of the samples—calculated from the adsorption branch and depicted in the inset of Figure 3—were

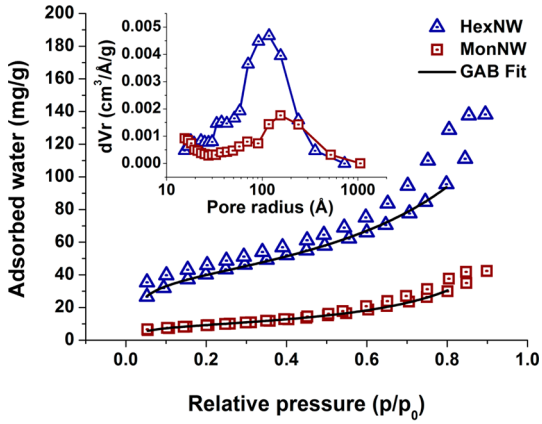

Figure 3. Water vapor adsorption−desorption isotherms of hexagonal and monoclinic nanowires. Solid lines are GAB fits to the adsorption branches. Inset represents the BJH pore size distribution of nanowires obtained from nitrogen sorption.

DOI: 10.1021/acsami.5b02177
ACS Appl. Mater. Interfaces 2015, 7, 9947−9956

similar, featuring a broad asymmetric peak centered at pore radius 11.0 and 17.3 nm for hexagonal and monoclinic nanowires, respectively. These pores clearly correspond to the interwire space as indicated by the correlation between their distributions and the TEM-based nanowire diameter distributions discussed above. The more pronounced low-diameter shoulder of the hexagonal nanowire PSD curve is due to the pores formed between the surface irregularities of bundled hexagonal nanowires. The water uptake capacity of the nanowires at different sorbate activities was also determined to gain insight into the underlying electrical conduction mechanism. Figure 3 depicts the water vapor sorption isotherms of hexagonal and monoclinic nanowires.

The adsorption branch of both nitrogen and water sorption isotherms were evaluated by the BET and GAB methods to estimate specific surface areas. Calculated values are summarized in Table 1.

Table 1. Specific Surface Area of Hexagonal and Monoclinic Nanowires Obtained from Nitrogen and Water Vapor Sorption Measurements via the GAB and BET Methods[a]

	$SSA_{H_2O}GAB$ (m^2/g)	$SSA_{H_2O}BET$ (m^2/g)	$SSA_{N_2}GAB$ (m^2/g)	$SSA_{N_2}BET$ (m^2/g)
HexNW	130.7 ± 7.9	119.1 ± 3.9	143.5 ± 3.4	130.2 ± 1.7
MonNW	30.4 ± 2.1	27.6 ± 0.3	62.0 ± 3.9	54.6 ± 0.7

[a]The SSA of hexagonal nanowires calculated from nitrogen sorption was ~2.3 times higher than that of monoclinic samples, while this factor increased to ~4.3 when calculated from the water sorption study.

The SSA values obtained by the GAB method are systematically higher than their BET counterparts. Deviations in surface areas obtained by the different methods are around ~10%. In both nitrogen and water vapor sorption studies hexagonal nanowires exhibited a considerably higher SSA because of their smaller average diameter and rougher surface; however, the factor between the SSA value pairs showed some difference. In the case of nitrogen sorption measurements hexagonal nanowires exhibited ~2.3 times higher surface area than monoclinic nanowires, while in the water sorption study this factor increased to ~4.3. It had been previously demonstrated by Fripiat and co-workers[38] that the determination of surface area using water vapor is less accurate than the evaluation of nitrogen sorption because the chemical nature of the surface plays a more pronounced role in the former than in the latter case. Therefore, the SSAs obtained from nitrogen sorption were used in further calculations.

Proton conductivity can be significantly altered by the chemical nature of the surface. Surface acidity, including the acid dissociation constant (pK_a) of individual or immobilized surface groups, has a profound impact on proton conductivity.[14,23,39−42] It was demonstrated that rare earth phosphates, especially cerium phosphate, have an inherent acidic character that can be utilized in catalysis.[43] Ammonia TPD is an established method to characterize the surface acidic centers of various compounds. The total ammonia uptakes of both nanowire types were determined by integrating the area under the TPD curves (not shown here). The ammonia consumption for hexagonal nanowires (0.58 mmol/g) was found to be twice as high as for the monoclinic one (0.25 mmol/g), suggesting a more acidic surface in the hexagonal structure. However, the SSA-corrected ammonia consumptions revealed practically identical surface coverages of 0.004 $mmol/m^2$ for both hexagonal and monoclinic nanowires. The number of ammonia molecules adsorbed onto 1 nm^2 of nanowire surface can readily be calculated by using the Avogadro constant and the cross-sectional area of the molecule (~14.0 $Å^2$).[33] The surface coverage of ammonia on both types of nanowires was found to be 2.4 $molecule/nm^2$, which is considerably less than the theoretical maximum of 7.1 $molecule/nm^2$ calculated from nitrogen adsorption experiments. Therefore, we conclude that $CePO_4$ nanowires have practically identical surface acidic center densities regardless of their crystal structures, and only part of the surface sites is available for ammonia adsorption.

Electrodynamic (impedance spectroscopy, IS) and electrostatic (isothermal transient ionic current, ITIC) methods were applied to examine the electrical properties. Figure 4 depicts

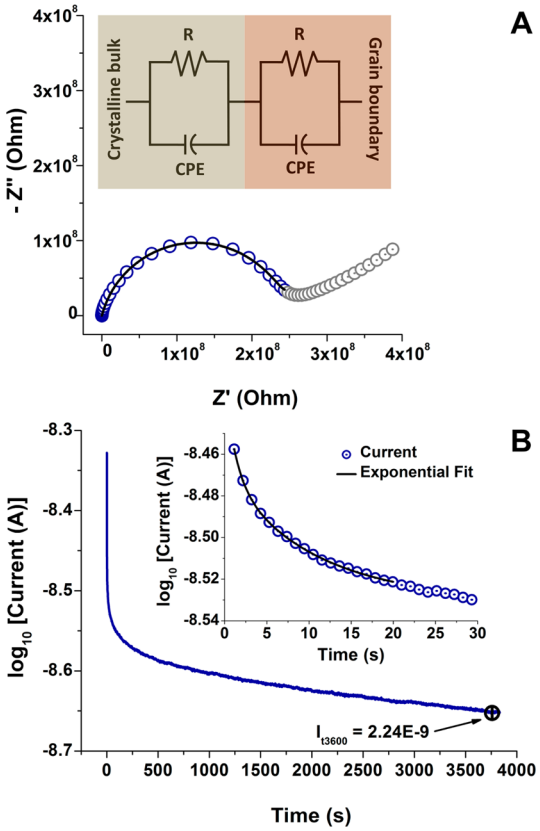

Figure 4. Determination of electrical conductivity by fitting the complex impedance spectrum (A). Inset shows the equivalent circuit used in the evaluation; the low-frequency region was omitted from fitting. Transient current curves were also used to obtain conductivity (B) by fitting the initial exponential decay (inset) and by recording residual current at 3600 s.

representative IS and ITIC curves of hexagonal nanowires at 33 RH%. The complex impedance spectrum is shown in Figure 4A as the so-called Nyquist diagram, where the negative of the imaginary part is plotted against its real part.

It is well-known that a single resistor−capacitor (RC) circuit consisting of purely resistive and capacitive components should give a symmetrical semicircle in the $-Im(Z^*)$ vs $Re(Z^*)$ plane, possessing a well-defined relaxation time corresponding to the Debye model. In nonideal systems it is rare to obtain an entirely symmetrical arc and usually a distorted and depressed semicircle forms. These systems cannot be characterized by one

DOI: 10.1021/acsami.5b02177
ACS Appl. Mater. Interfaces 2015, 7, 9947−9956

distinct relaxation time, but rather by the distribution of a series of relaxation times. Consequently, the purely capacitive component of the RC circuit is generally replaced by a constant phase element (CPE). In our case the complex impedance spectrum was suitably modeled by the equivalent circuit of two R-CPE parallel circuits connected in series (Figure 4A inset) assuming that crystalline-bulk and grain-boundary related charge-transfer processes can be accounted for by the development of the asymmetrical, depressed semicircle. This model was successfully applied to interpret many similar nonideal systems consisting of randomly oriented, interconnected particles and ceramics with grain boundaries.[7,16,44−46] The impedance of the above equivalent circuit was expressed by the sum of two Cole−Cole equations,

$$Z = \frac{R_{gb}}{1 + (i\omega\tau_{gb})^{\alpha_{gb}}} + \frac{R_{cr}}{1 + (i\omega\tau_{cr})^{\alpha_{cr}}} \quad (3)$$

where "gb" and "cr" correspond to grain boundary and crystalline phase, R denotes resistance, i is the imaginary unit, α is the CPE exponent ($0 < \alpha < 1$), ω is the angular frequency, and τ is the relaxation time. Conductivity of the samples was derived from the cumulative resistance values obtained from the fit of the Nyquist plots. The low-frequency region was excluded from the fitting and was not interpreted in detail due to the ambiguous interpretation of its origin in the literature. Typical explanations for this phenomenon were suggested to be a diffusion limited charge-transfer process at low frequencies (commonly described by the Warburg diffusion element) or the so-called low-frequency dispersion (or quasi dc conductivity), which might originate from electrochemical reactions on the electrode−sample interfaces or hopping-type electronic conduction as suggested by Jonscher and another.[47,48] At low frequency the buildup of the electrochemical double layer (i.e., electrode polarization) also takes place, further hindering the evaluation of the region. As a mathematical description, a constant phase element is often used with $\alpha = 0.5$ in the case of Warburg diffusion and $0 < \alpha < 1$ in the case of low-frequency dispersion.

To further support our impedance spectroscopic results, an alternative chronoamperometric technique was applied as well. Figure 4B shows a representative current response after applying a potential step from 0 to 3 V in hexagonal $CePO_4$ nanowires at 33 RH%. Conductivity from ITIC measurement was obtained by fitting the current decay to

$$I(t) = \frac{A\sigma_{dc}U}{d} \exp\left(-\frac{\mu U}{d^2}t\right) \quad (4)$$

where A is the electrode surface area, d is the electrode spacing, σ_{dc} is the dc conductivity, t is the time elapsed after the onset of the potential U, and μ is the mobility of ionic charge carriers. Alternatively, the residual current at $t = 3600$ s was also extracted from the experimental data set.

Figure 5A shows the conductivity derived from IS and ITIC investigations for monoclinic and hexagonal nanowires as a function of the relative humidity of the atmosphere.

At low relative humidity, hexagonal nanowires exhibited around 2 orders of magnitude higher conductivity than monoclinic ones. With exposure of the samples to higher relative humidity conditions, the conductivity differences gradually disappeared, and above 80 RH% all samples had almost identical conductivity. One order of magnitude difference was observed between ITIC and IS results

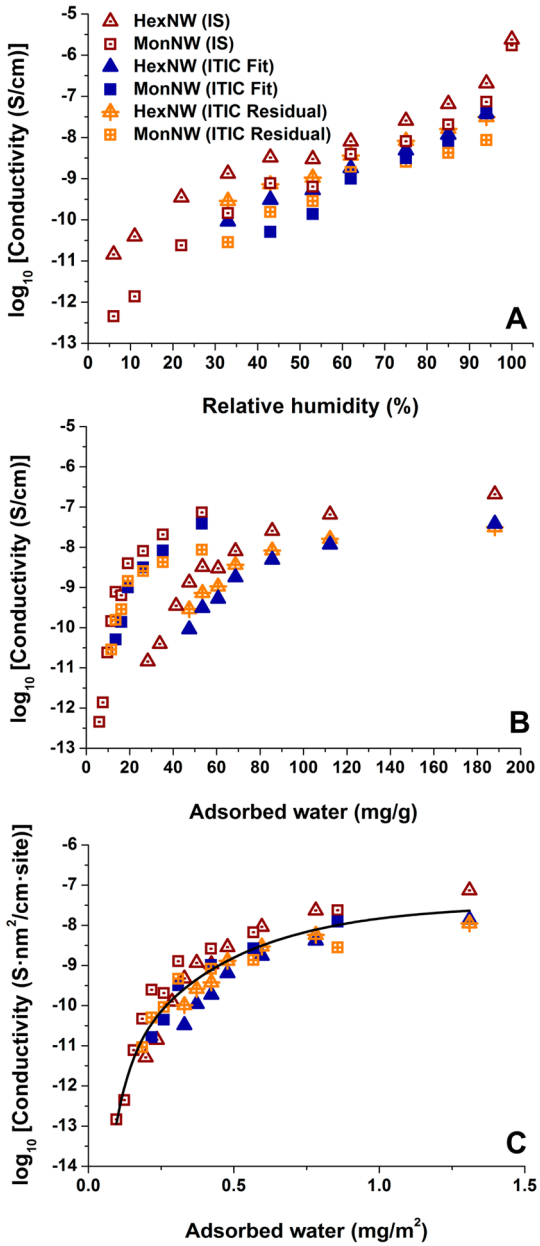

Figure 5. Conductivities of hexagonal and monoclinic nanowires derived from IS and ITIC depicted as a function of relative humidity (A), absorbed amount of water (B), and surface area corrected adsorbed amount of water (C). Conductivity vs relative humidity showed higher values for hexagonal nanowires at low RH% values but the difference was reduced as higher RH% were applied. Conductivity as a function of adsorbed water amount exhibited the opposite tendency: monoclinic nanowires had almost 3 times higher conductivity at a desired adsorbed amount (especially at low RH% values). However, as soon as conductivity was normalized to the number density of surface acidic sites, all differences disappeared and the conductivity curves collapsed into one master curve.

throughout the investigated relative humidity range, which is a well-known phenomenon in the comparison of values derived from IS and ITIC measurements.[49]

Although Figure 5A provides the best illustration for comparing the humidity sensitivity of the samples from an application point of view, some additional representations were utilized to shed light on the details of the conductivity differences. When conductivity was depicted as a function of

DOI: 10.1021/acsami.5b02177
ACS Appl. Mater. Interfaces 2015, 7, 9947−9956

absolute adsorbed water amount, saturation curves appeared (Figure 5B). In this representation monoclinic nanowires had 3 orders of magnitude higher conductivity at low adsorbed amounts than their hexagonal counterparts, showing a tendency opposite to that shown in Figure 5A. Therefore, monoclinic nanowires had to be exposed to much higher relative humidity to adsorb the same amount of water as hexagonal nanowires; e.g., a RH% of 6 and 75 was necessary to achieve an adsorbed amount of ~30 mg/g for hexagonal and monoclinic nanowires, respectively. Since the specific surface area of monoclinic nanowires is lower than that of hexagonal nanowires (more than 4.3 according to water vapor and 2.3 times from nitrogen sorption study), ~30 mg/g of adsorbed water can build up a contiguous layer or even multilayers on their surface. The same amount of water on hexagonal nanowires was presumably not sufficient even for the formation of monolayer coverage, and thus separated water islands are formed at 6 RH%. It should also be taken into account that ~2−3 times higher amounts of adsorbed water were needed on hexagonal nanowires to reach the same conductivity as on monoclinic nanowires. For instance, 2×10^{-8} S/cm conductivity was observed at 85 mg/g of adsorbed water on hexagonal nanowires, while monoclinic wires reached this value already at 35 mg/g. The observed ~2.4-fold factor difference between the adsorbed amounts correlates well with the difference in specific surface areas (~2.3-fold), implying that surface area plays an important role in the conduction processes.

To prove the latter hypothesis, conductivity values were normalized by surface area, taking surface acidic centers into account. Figure 5C depicts the conductivity of unit surface acid density (number of acidic centers per area unit) as a function of the amount adsorbed by unit specific surface area (adsorbed amount divided by the nanowires' surface areas) obtained from nitrogen sorption experiment. In this representation all curves collapsed into a single master curve, which is characteristic of $CePO_4$ nanowires regardless of their crystal structure. These results provide further proof on the substantial role of surface acidic sites in conduction processes as suggested extensively in the literature.[39]

It is seen in Figure 6A that relaxation times decreased by 4 orders of magnitude with increasing amounts of adsorbed water in both samples, displaying exponential curvature similar to the conductivity as discussed above.

To examine the interrelation between the observed dielectric processes (the two relaxations and the conductivity) in $CePO_4$ nanowires, relaxation times were first plotted against conductivity in Figure 6B and then against each other in Figure 6C. Time constants in Figure 6B were normalized to τ at $\log_{10}(\sigma) = -10$ for the ease of comparison. The resulting linear dependence in the developed master curves with slopes of unity clearly indicates close connection between these seemingly independent processes. The identical dependence of relaxation times on conductivity implies a common origin of conduction, and the interdependency in Figure 6C suggests that we simply observe the same process from different perspectives as was put forward earlier for hydrophilic titanate nanowires.[50] However, the origin of the relaxations is the topic of an ongoing debate in the literature and various, often contradictory, assignments can be found; dipolar relaxation of adsorbate molecules, charge accumulation at interfaces, and relaxation of ionic species were all suggested before.[49,51−54]

The CPE exponent (α) in eq 3 accounts for the degree of depression of the semicircle on the complex impedance plane

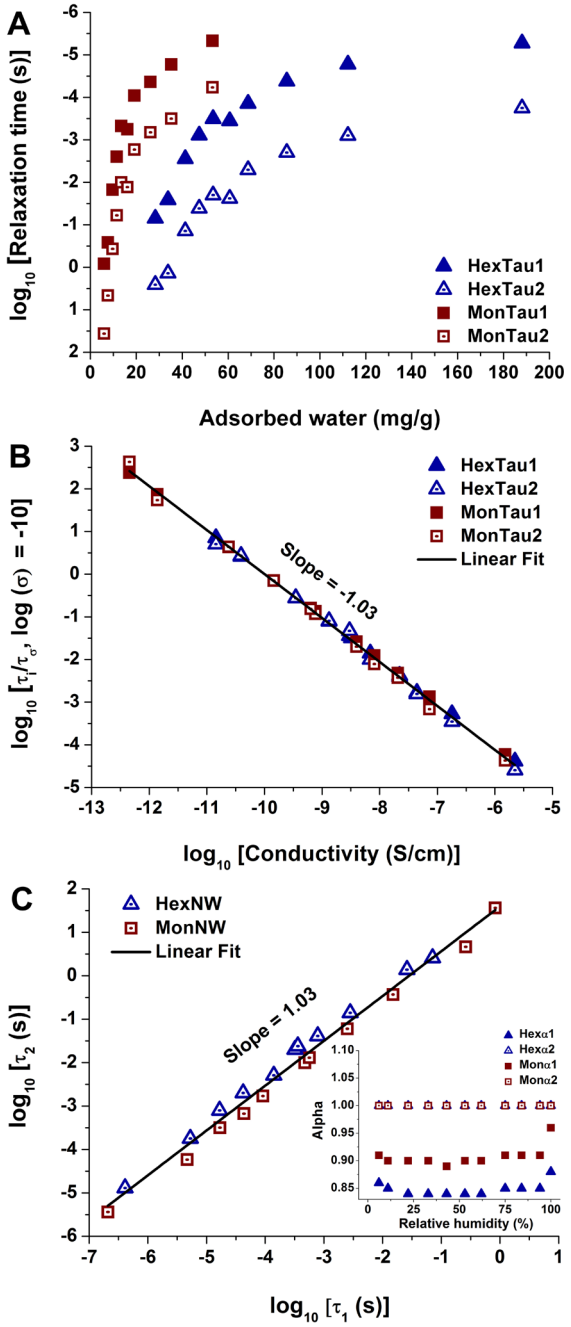

Figure 6. Variation of relaxation times with increasing amount of adsorbed water (A), the interrelation between conductivity and relaxations (B), and between the two respective relaxation processes (C). The linear dependencies with slopes close to 1 imply inherent connection between the three dielectric processes. The inset in part C depicts the variation of the CPE exponent (α) as a function of relative humidity.

in the Nyquist formalism. In the case of $\alpha = 1$ the sample behaves as an ideal capacitor; however, in nonideal systems its value usually falls into the range of 0.8−1. Analyzing the parameters of the applied equivalent circuit, a value of unity was obtained for the crystalline contribution (α_{cr}) in both samples; thus, the second term in eq 3 could be replaced by a simple RC circuit.[7] The first term of the equation, related to the grain boundary contribution, possessed $\alpha \approx 0.85$ in hexagonal nanowires and $\alpha \approx 0.9$ in monoclinic nanowires. CPE behavior is well-known in the literature and is widely used to interpret

DOI: 10.1021/acsami.5b02177
ACS Appl. Mater. Interfaces 2015, 7, 9947−9956

the impedance response of various systems, even though its origin is still a topic of debate. Fractal geometry or the micro-/nanoscale inhomogeneity of the electrode surface, adsorption of ionic impurities, evolution of nonuniform diffusion, and the nonuniform current distribution along the electrode surface were suggested to explain the emergence of relaxation times distribution.[55] Further studies proved that higher surface area and more dispersed adsorption of ions are favorable for the increase of α,[56] while other investigations on powders identified surface roughness, grain size, and grain boundary contribution as potential origins of the phenomenon.[55,57,58] Jorcin and co-workers found that the distribution of time constants along the electrode surface or in the direction perpendicular to it could serve as common explanations for the emergence of CPE behavior.[59,60] Though many contradictions can be found in the literature regarding the origin of CPE behavior, it can be presumed that in an inhomogeneous system like a heap of randomly interconnected $CePO_4$ nanowires of varying size and surface roughness the distribution of time constants will also occur.

To supplement TPD measurements, potentiometric titration of $CePO_4$ nanowires was performed to determine the net proton consumption of the samples. NaCl solutions with concentrations of 0.005, 0.05, and 0.5 M were used to determine the variation in the net proton consumption of the samples as a function of the varying ionic strength of the background electrolyte. Figure 7 depicts the net proton consumption vs pH curves for each ionic strength. Regardless of the crystal structure, the three curves determined at different background electrolyte concentrations with increasing pH (U curve series) intersected at a proton consumption of around −0.05 mmol/g. This indicates that processes other than surface charging were also involved in the protonation/deprotonation reactions. When the net proton consumption curves were further examined, a hysteresis loop could be discerned in the pH range of ∼6−10. In general, these observations point to the possibility of acidic contamination in the samples.[34]

In our case, phosphoric acid was used as the phosphate source for the synthesis of the cerium phosphate nanowires. Despite the thorough washing procedure applied, it is likely that some phosphoric acid residue from the synthesis remained adsorbed on the nanowire surface. A similar observation was made in the synthesis of lanthanum phosphate precipitate earlier.[61] It was proved that phosphoric acid contamination can only be removed completely by heat treatment at 1400 °C (at this temperature it undergoes decomposition). Nevertheless, thorough washing with distilled water and ethanol is the standard literature procedure for the cleaning of the $CePO_4$ nanowires, even though it seems inadequate for the total elimination of adsorbed phosphoric acid. Therefore, we also followed this approach to keep our results comparable with literature data. Furthermore, the suggested calcination process would induce undesired transformations in nanowire morphology and crystal structure,[30,62] which would make any further comparison uncertain.

Considerable positive proton consumption under pH ∼4.5 could be observed in both samples. Considering the potentiometric titration study of $FePO_4$, the following surface protonation/deprotonation processes could be suggested for the $CePO_4$ system:[63]

$$\equiv Ce{-}OH_2^+ \leftrightarrow \equiv Ce{-}OH + H^+ \leftrightarrow \equiv Ce{-}O^- + 2H^+$$

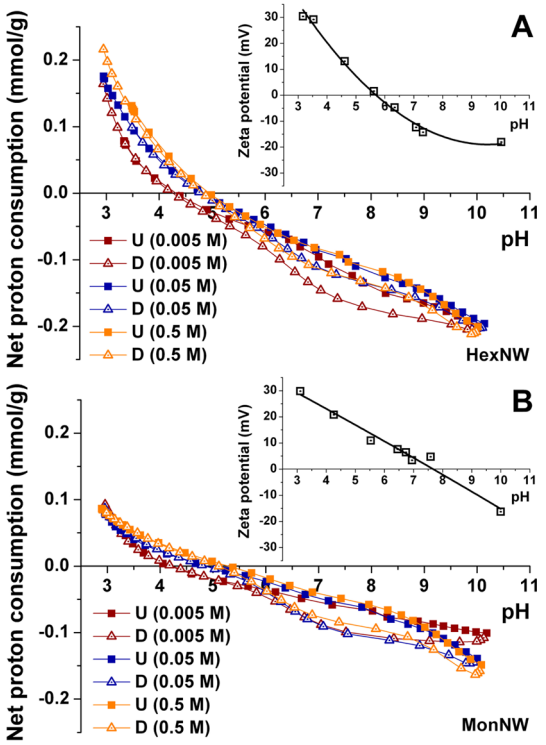

Figure 7. pH-dependent net proton consumption of hexagonal (A) and monoclinic (B) nanowires. In both cases the curves recorded at different background electrolyte concentrations intersect at around −0.05 mmol/g consumed value. Each curve featured a hysteresis loop between pH 6 and pH 10. These observations indicate the presence of residual adsorbed phosphoric acid in the samples. Below pH ∼ 4.5 considerable positive proton consumptions were observed, referring to the development of $\equiv Ce{-}OH_2^+$ species on the surface, confirmed by zeta potential measurements shown in insets. Below pH ∼ 3.5 the slow dissolution of the nanowires (rather conspicuous in hexagonal nanowires) was indicated. U and D labels refer to the "up" (increasing pH) and "down" (decreasing pH) parts of the titrations, respectively.

$$>P{-}OH \leftrightarrow >P{-}O^- + H^+ \quad (5)$$

Pursuant to this model, it is likely that under pH ∼ 4.5 the positive surface charge mainly stems from the development of $\equiv Ce{-}OH_2^+$ species. The existence of such positively charged sites on the surface was also confirmed by zeta potential measurements shown in the insets of Figure 7, where the point of zeta potential sign reversal occurs at pH ∼ 5.5 and pH ∼ 7.5 for hexagonal and monoclinic nanowires, respectively. It is worth noting that the difference between the pHs where the zeta potential functions and net proton consumption curves intersect the pH axis for both samples (about 1 and 2 pH unit for HexNW and MonNW, respectively) also suggests the presence of acidic impurities: net proton consumptions become zero at lower pHs than that of the zeta potential reversal.

It is also apparent that the slow dissolution of cerium phosphate was commenced under pH ∼ 3, which is conspicuous especially in the case of hexagonal nanowires. The net proton consumption of the protonated surfaces was determined at pH ∼ 4 to avoid the effect of any dissolution process. At 0.005 M background electrolyte concentration the consumed proton amounts were 0.018 mmol/g for hexagonal and 0.008 mmol/g for monoclinic nanowires. When the concentration of the background electrolyte is raised to 0.5 M, the proton consumptions also increased due to the charge

DOI: 10.1021/acsami.5b02177
ACS Appl. Mater. Interfaces 2015, 7, 9947−9956

screening effect of chloride ions. In this case, hexagonal and monoclinic nanowires consumed 0.074 and 0.034 mmol/g protons, respectively. When the proton consumption of hexagonal nanowires is divided by the proton consumption of monoclinic nanowires, practically identical factors of 2.3 (0.005 M) and 2.2 (0.5 M) were obtained, which indicates that the ratio between proton consumptions of the samples is independent of the ionic strength at pH ∼ 4. This observation suggests that the ≡Ce−OH sites show similar behavior irrespective of the crystal structure. Since the protonation of ≡Ce−OH sites to the highest degree is the most likely at the highest electrolyte concentration at pH ∼ 4.0, the proton consumptions recorded in the 0.5 M background solution were used for further calculations. Similarly to TPD results, SSA-corrected proton consumptions showed practically identical values of 5.2×10^{-4} mmol/m^2 for hexagonal and 5.5×10^{-4} mmol/m^2 for monoclinic nanowires. Thus, the potentiometric titration results showed 1 order of magnitude difference from TPD values, which may arise from the incomplete protonation of ≡Ce−OH sites. This is most likely due to the local repulsion forces between adjacent positive charges. Presumably, only 10% of the total ≡Ce−OH sites became positively charged by the end of the protonation process, as was reported earlier by James and Parks.[64] After this correction is applied, the TPD and potentiometric titration results correlate very well.

Summarizing, studying the surface properties of structurally different $CePO_4$ nanowires with independent methods revealed that electric conduction in ambient-temperature solid-state proton conductors is due to a fundamentally identical, crystal-structure-independent proton-transport mechanism. We believe that our finding is a step forward toward better understanding of the low-temperature proton conduction mechanism, which may eventually contribute to the development of more efficient fuel-cell membranes.

4. CONCLUSION

The charge-transport properties of one-dimensional monoclinic and hexagonal cerium phosphate nanowires were studied by impedance spectroscopy and transient ionic current methods. The structural and surface properties of nanowires were investigated by high-resolution transmission electron microscopy, X-ray diffractometry, nitrogen and water sorption, temperature-programmed ammonia desorption, and potentiometric titration techniques. Examining the interrelation between proton transport and surface structure helps further clarify some details of the conduction mechanism in solid-state proton conductors.

Charge-transport and electric relaxation processes were identified dependent impedance measurements performed on samples kept at varying relative humidity, and were quantitatively characterized by fitting impedance spectra with an appropriate equivalent circuit. The differences in the obtained raw conductivity vs humidity plots diminished when specific surface area and acid center density were also taken into account, and the initially distinct characteristics collapsed into one master curve. Combining these observations with further investigations on surface acidity indicated a crystal-structure-independent conduction mechanism in $CePO_4$ nanowires. These findings will contribute to a better understanding of charge-transport phenomena in low-temperature proton conduction materials, relevant in the development of advanced fuel-cell membranes.

■ ASSOCIATED CONTENT

Supporting Information

EDS spectra and nitrogen sorption isotherm of hexagonal and monoclinic nanowires. This material is available free of charge via the Internet at http://pubs.acs.org/.

■ AUTHOR INFORMATION

Corresponding Author

*E-mail: konya@chem.u-szeged.hu.

Notes

The authors declare no competing financial interest.

■ ACKNOWLEDGMENTS

The financial support of the Hungarian National Research Fund projects OTKA NN 110676, K 112531, and TÁMOP 4.2.4.A/2-11-1-2012-0001 is acknowledged. Authors would also like to thank Kornélia Baán for TPD measurements.

■ REFERENCES

(1) Bockris, J. Hydrogen Economy Is Possible by 1990s. *Chem. Eng. News* **1977**, *55*, 27−30.
(2) Gregory, D. The Hydrogen Economy Concept. *AIP Conf. Proc.* **1974**, *19*, 171−174.
(3) Crabtree, G. W.; Dresselhaus, M. S.; Buchanan, M. V. The Hydrogen Economy. *Phys. Today* **2004**, *57*, 39−44.
(4) Devanathan, R. Recent Developments in Proton Exchange Membranes for Fuel Cells. *Energy Environ. Sci.* **2008**, *1*, 101−119.
(5) Brandon, N. P.; Skinner, S.; Steele, B. C. H. Recent Advances in Materials for Fuel Cells. *Annu. Rev. Mater. Res.* **2003**, *33*, 183−213.
(6) Truffier-Boutry, D.; De Geyer, A.; Guetaz, L.; Diat, O.; Gebel, G. Structural Study of Zirconium Phosphate−Nafion Hybrid Membranes for High-Temperature Proton Exchange Membrane Fuel Cell Applications. *Macromolecules* **2007**, *40*, 8259−8264.
(7) Stankiewicz, J.; Tomás, M.; Dobrinovitch, I. T.; Forcén-Vázquez, E.; Falvello, L. R. Proton Conduction in a Nonporous One Dimensional Coordination Polymer. *Chem. Mater.* **2014**, *26*, 5282−5287.
(8) Ogawa, T.; Kamiguchi, K.; Tamaki, T.; Imai, H.; Yamaguchi, T. Differentiating Grotthuss Proton Conduction Mechanisms by Nuclear Magnetic Resonance Spectroscopic Analysis of Frozen Samples. *Anal. Chem.* **2014**, *86*, 9362−9366.
(9) Ogawa, T.; Aonuma, T.; Tamaki, T.; Ohashi, H.; Ushiyama, H.; Yamashita, K.; Yamaguchi, T. The Proton Conduction Mechanism in a Material Consisting of Packed Acids. *Chem. Sci.* **2014**, *5*, 4878−4887.
(10) Ogawa, T.; Ushiyama, H.; Lee, J.-M.; Yamaguchi, T.; Yamashita, K. Theoretical Studies on Proton Transfer among a High Density of Acid Groups: Surface of Zirconium Phosphate with Adsorbed Water Molecules. *J. Phys. Chem. C* **2011**, *115*, 5599−5606.
(11) Ogawa, T.; Ohashi, H.; Tamaki, T.; Yamaguchi, T. Non-Humidified Proton Conduction between a Lewis Acid-Base Pair. *Phys. Chem. Chem. Phys.* **2013**, *15*, 13814−13817.
(12) Li, Z.; He, G.; Zhang, B.; Cao, Y.; Wu, H.; Jiang, Z.; Tiantian, Z. Enhanced Proton Conductivity of Nafion Hybrid Membrane under Different Humidities by Incorporating Metal−Organic Frameworks with High Phytic Acid Loading. *ACS Appl. Mater. Interfaces* **2014**, *6*, 9799−9807.
(13) Jin, Y. G.; Qiao, S. Z.; Xu, Z. P.; Yan, Z.; Huang, Y.; Diniz da Costa, J. C.; Lu, G. Q. Phosphonic Acid Functionalized Silicas for Intermediate Temperature Proton Conduction. *J. Mater. Chem.* **2009**, *19*, 2363−2372.
(14) Steininger, H.; Schuster, M.; Kreuer, K. D.; Kaltbeitzel, A.; Bingol, B.; Meyer, W. H.; Schauff, S.; Brunklaus, G.; Maier, J.; Spiess, H. W. Intermediate Temperature Proton Conductors for Pem Fuel Cells Based on Phosphonic Acid as Protogenic Group: A Progress Report. *Phys. Chem. Chem. Phys.* **2007**, *9*, 1764−1773.

DOI: 10.1021/acsami.5b02177
ACS Appl. Mater. Interfaces 2015, 7, 9947−9956

(15) Sun, X.; Wang, S.; Wang, Z.; Ye, X.; Wen, T.; Huang, F. Proton Conductivity of CeP_2O_7 for Intermediate Temperature Fuel Cells. *Solid State Ionics* **2008**, *179*, 1138−1141.
(16) Le, M.-V.; Tsai, D.-S.; Yang, C.-Y.; Chung, W.-H.; Lee, H.-Y. Proton Conductors of Cerium Pyrophosphate for Intermediate Temperature Fuel Cell. *Electrochim. Acta* **2011**, *56*, 6654−6660.
(17) Thakkar, R.; Chudasama, U. Synthesis, Characterization and Proton Transport Properties of a Mixed Material—Zirconium Titanium Phosphate, a Tetravalent Bimetallic Acid Salt. *Electrochim. Acta* **2009**, *54*, 2720−2726.
(18) Hogarth, W. H. J.; Muir, S. S.; Whittaker, A. K.; Diniz da Costa, J. C.; Drennan, J.; Lu, G. Q. Proton Conduction Mechanism and the Stability of Sol−Gel Titanium Phosphates. *Solid State Ionics* **2007**, *177*, 3389−3394.
(19) Alberti, G.; Casciola, M.; Cavalaglio, S.; Vivani, R. Proton Conductivity of Mesoporous Zirconium Phosphate Pyrophosphate. *Solid State Ionics* **1999**, *125*, 91−97.
(20) Haile, S. M.; Liu, H.; Secco, R. A. High-Temperature Behavior of CsH_2PO_4 under Both Ambient and High Pressure Conditions. *Chem. Mater.* **2003**, *15*, 727−736.
(21) Swint, A. L.; Bohn, P. W. Effect of the Interfacial Chemical Environment on in-Plane Electronic Conduction of Indium Tin Oxide: Role of Surface Charge, Dipole Magnitude, and Carrier Injection. *Langmuir* **2004**, *20*, 4076−4084.
(22) Jiang, S. P. Functionalized Mesoporous Structured Inorganic Materials as High Temperature Proton Exchange Membranes for Fuel Cells. *J. Mater. Chem. A* **2014**, *2*, 7637−7655.
(23) Vichi, F. M.; Tejedor-Tejedor, M. I.; Anderson, M. A. Effect of Pore-Wall Chemistry on Proton Conductivity in Mesoporous Titanium Dioxide. *Chem. Mater.* **2000**, *12*, 1762−1770.
(24) Costantino, F.; Donnadio, A.; Casciola, M. Survey on the Phase Transitions and Their Effect on the Ion-Exchange and on the Proton-Conduction Properties of a Flexible and Robust Zr Phosphonate Coordination Polymer. *Inorg. Chem.* **2012**, *51*, 6992−7000.
(25) Nagao, M.; Kamiya, T.; Heo, P.; Tomita, A.; Hibino, T.; Sano, M. Proton Conduction in In^{3+}-Doped SnP_2O_7 at Intermediate Temperatures. *J. Electrochem. Soc.* **2006**, *153*, A1604−A1609.
(26) Toyoura, K.; Hatada, N.; Nose, Y.; Tanaka, I.; Matsunaga, K.; Uda, T. Proton-Conducting Network in Lanthanum Orthophosphate. *J. Phys. Chem. C* **2012**, *116*, 19117−19124.
(27) Phadke, S.; Nino, J. C.; Islam, M. S. Structural and Defect Properties of the $LaPO_4$ and LaP_5O_{14}-Based Proton Conductors. *J. Mater. Chem.* **2012**, *22*, 25388−25394.
(28) Kitamura, N.; Amezawa, K.; Tomii, Y.; Yamamoto, N. Protonic Conduction in Rare Earth Orthophosphates with the Monazite Structure. *Solid State Ionics* **2003**, *162*−*163*, 161−165.
(29) Amezawa, K.; Maekawa, H.; Tomii, Y.; Yamamoto, N. Protonic Conduction and Defect Structures in Sr-Doped $LaPO_4$. *Solid State Ionics* **2001**, *145*, 233−240.
(30) Pusztai, P.; Kukovecz, A.; Konya, Z. Green Synthesis of Biomimetic $CePO_4$:Tb Nanostructures Using the Simplest Morphology Control. *RSC Adv.* **2014**, *4*, 49879−49887.
(31) Brunauer, S.; Emmett, P. H.; Teller, E. Adsorption of Gases in Multimolecular Layers. *J. Am. Chem. Soc.* **1938**, *60*, 309−319.
(32) Timmermann, E. O. Multilayer Sorption Parameters: BET or GAB Values? *Colloids Surf., A* **2003**, *220*, 235−260.
(33) McClellan, A. L.; Harnsberger, H. F. Cross-Sectional Areas of Molecules Adsorbed on Solid Surfaces. *J. Colloid Interface Sci.* **1967**, *23*, 577−599.
(34) Szekeres, M.; Tombácz, E. Surface Charge Characterization of Metal Oxides by Potentiometric Acid−Base Titration, Revisited Theory and Experiment. *Colloids Surf., A* **2012**, *414*, 302−313.
(35) Cao, X.; Xie, Y.; Li, L. Crystallization of Amorphous Colloids: An Effective Approach for the Rapid and Large-Scale Preparation of Antimony Sulfide Dendrites. *J. Solid State Chem.* **2004**, *177*, 202−206.
(36) Huang, C. H. *Rare Earth Coordination Chemistry: Fundamentals and Applications*, 1st ed.; Wiley: Singapore, 2010.
(37) Morss, L. R.; Edelstein, N. M.; Fuger, J. *The Chemistry of the Actinide and Transactinide Elements*, 4th ed.; Springer: Dordrecht, The Netherlands, 2011.
(38) Fripiat, J. J.; Jelli, A.; Poncelet, G.; André, J. Thermodynamic Properties of Adsorbed Water Molecules and Electrical Conduction in Montmorillonites and Silicas. *J. Phys. Chem.* **1965**, *69*, 2185−2197.
(39) Bibent, N.; Mehdi, A.; Silly, G.; Henn, F.; Devautour-Vinot, S. Proton Conductivity Versus Acidic Strength of One-Pot Synthesized Acid-Functionalized SBA-15 Mesoporous Silica. *Eur. J. Inorg. Chem.* **2011**, *2011*, 3214−3225.
(40) Kreuer, K.-D. Proton Conductivity: Materials and Applications. *Chem. Mater.* **1996**, *8*, 610−641.
(41) Hara, S.; Takano, S.; Miyayama, M. Proton-Conducting Properties and Microstructure of Hydrated Tin Dioxide and Hydrated Zirconia. *J. Phys. Chem. B* **2004**, *108*, 5634−5639.
(42) Planchais, A.; Devautour-Vinot, S.; Salles, F.; Ragon, F.; Devic, T.; Serre, C.; Maurin, G. A Joint Experimental/Computational Exploration of the Dynamics of Confined Water/Zr-Based MOFs Systems. *J. Phys. Chem. C* **2014**, *118*, 14441−14448.
(43) Onoda, H.; Nariai, H.; Moriwaki, A.; Maki, H.; Motooka, I. Formation and Catalytic Characterization of Various Rare Earth Phosphates. *J. Mater. Chem.* **2002**, *12*, 1754−1760.
(44) Ren, F.; Ling, Y.; Feng, J. The Role of W Doping in Response of Hydrogen Sensors Based on MAO Titania Films. *Appl. Surf. Sci.* **2010**, *256*, 3735−3739.
(45) Bhella, S. S.; Kuti, L. M.; Li, Q.; Thangadurai, V. Electrical Transport Properties of in-Doped $Ce_{1-x}In_xO_{2-\delta}$ (x = 0.1; 0.2). *Dalton Trans.* **2009**, 9520−9528.
(46) Karoui, K.; Rhaiem, A. B.; Hlel, F.; Arous, M.; Guidara, K. Dielectric and Electric Studies of the $[N(CH_3)_4][N(C_2H_5)_4]ZnCl_4$ Compound at Low Temperature. *Mater. Chem. Phys.* **2012**, *133*, 1−7.
(47) Andrew, K. J. Dielectric Relaxation in Solids. *J. Phys. D: Appl. Phys.* **1999**, *32*, R57−R70.
(48) Jonscher, A. K. *Dielectric Relaxation in Solids*, 1st ed.; Chelsea Dielectrics: London, 1983.
(49) Haspel, H.; Laufer, N.; Bugris, V.; Ambrus, R.; Szabó-Révész, P.; Kukovecz, Á. Water-Induced Charge Transport Processes in Titanate Nanowires: An Electrodynamic and Calorimetric Investigation. *J. Phys. Chem. C* **2012**, *116*, 18999−19009.
(50) Haspel, H.; Bugris, V.; Kukovecz, Á. Water Sorption Induced Dielectric Changes in Titanate Nanowires. *J. Phys. Chem. C* **2013**, *117*, 16686−16697.
(51) Zachariah, M.; Mitsari, E.; Romanini, M.; Zygouri, P.; Gournis, D.; Barrio, M. D.; Tamarit, J. L.; Macovez, R. Water-Triggered Conduction Mediated by Proton Exchange in a Hygroscopic Fulleride and Its Hydrate. *J. Phys. Chem. C* **2015**, *119*, 685−694.
(52) Macovez, R.; Mitsari, E.; Zachariah, M.; Romanini, M.; Zygouri, P.; Gournis, D.; Tamarit, J. L. Ultraslow Dynamics of Water in Organic Molecular Solids. *J. Phys. Chem. C* **2014**, *118*, 4941−4950.
(53) Cerveny, S.; Schwartz, G. A.; Otegui, J.; Colmenero, J.; Loichen, J.; Westermann, S. Dielectric Study of Hydration Water in Silica Nanoparticles. *J. Phys. Chem. C* **2012**, *116*, 24340−24349.
(54) Sáiz, L. M.; Cerveny, S. Dynamics of Amorphous and Partially Crystallized Proline Solutions. *J. Non-Cryst. Solids* **2015**, *407*, 486−493.
(55) Barsoukov, E.; Macdonald, J. R. *Impedance Spectroscopy: Theory, Experiment, and Applications*, 2nd ed.; Wiley: Hoboken, NJ, 2005.
(56) Lasia, A. *Electrochemical Impedance Spectroscopy and Its Applications*, 1st ed.; Springer: New York, 2014.
(57) Huang, K.; Tichy, R. S.; Goodenough, J. B. Superior Perovskite Oxide-Ion Conductor; Strontium- and Magnesium-Doped $LaGaO_3$: Ii, Ac Impedance Spectroscopy. *J. Am. Ceram. Soc.* **1998**, *81*, 2576−2580.
(58) Park, J.-H.; Kim, C.-S.; Choi, B.-C.; Jeong, J.-H.; Moon, B. K.; Seo, H.-J.; Kim, I.-W.; Kim, J.-S. Electrical Properties of Pulsed Laser-Deposited $Sr_xBi_yTa_2O_9$ Thin Films on Bi/Sr Ratios. *Solid State Commun.* **2003**, *127*, 315−318.
(59) Jorcin, J.-B.; Orazem, M. E.; Pébère, N.; Tribollet, B. CPE Analysis by Local Electrochemical Impedance Spectroscopy. *Electrochim. Acta* **2006**, *51*, 1473−1479.

DOI: 10.1021/acsami.5b02177
ACS Appl. Mater. Interfaces 2015, 7, 9947−9956

(60) Lvovich, V. F. *Impedance Spectroscopy: Applications to Electrochemical and Dielectric Phenomena*, 1st ed.; Wiley: Hoboken, NJ, 2012.
(61) Lucas, S.; Champion, E.; Bernache-Assollant, D.; Leroy, G. Rare Earth Phosphate Powders $RePO_4{\cdot}nH_2O$ (Re = La, Ce or Y) Ii. Thermal Behavior. *J. Solid State Chem.* **2004**, *177*, 1312−1320.
(62) Pusztai, P.; Simon, T.; Kukovecz, Á.; Kónya, Z. Structural Stability Test of Hexagonal $CePO_4$ Nanowires Synthesized at Ambient Temperature. *J. Mol. Struct.* **2013**, *1044*, 94−98.
(63) De Tommaso, G.; Iuliano, M. Acid−Base Properties of the Surface of Hydrous Ferric Phosphate in Aqueous Solutions. *J. Chem. Eng. Data* **2011**, *57*, 52−59.
(64) James, R.; Parks, G. Characterization of Aqueous Colloids by Their Electrical Double-Layer and Intrinsic Surface Chemical Properties. In *Surface and Colloid Science*, 1st ed.; Matijević, E., Ed.; Springer: New York, 1982; Chapter 2, pp 119−216.

DOI: 10.1021/acsami.5b02177
ACS Appl. Mater. Interfaces 2015, 7, 9947−9956